Supporting Information

Amine Functionalized Surface Frustrated Lewis Pairs Boost CO_2 Photocatalysis

Qinhui Guan, Chengzhe Ni, Tingjiang Yan*, Na Li*, Lu Wang, Zhe Lu, Weiguang Ran, Yipin Zhang, Wenjuan Li, Lulu Zhang, Dapeng Zhang, Baibiao Huang, Geoffrey A. Ozin*

Table of Content

1. EXPERIMENTAL SECTION

1.1. Catalyst Synthesis.

1.1.1. Chemicals and materials

The $In(NO_3)_3 \cdot xH_2O$ ($\geq$ 99.9 %) was purchased from Aladdin Chemical Reagent Co., ltd. NaOH, ethylenediamine (EDA, $\geq$ 99.0 %), tetraethyl orthosilicate (TEOS, the equivalent SiO_2 content is 28.4 %), ethanol ($\geq$ 99.7 %), ammonia (25~28 wt% in water) were purchased from Sinopharm Co., ltd. All reagents used were analytical grade without any further purification. Additionally, throughout the entire experimental process, the deionized (DI) water used was self-prepared using an ultrapure water system of our laboratory. The synthesis methods of all samples are illustrated in Scheme S1.

1.1.2. Synthesis of regular In₂O₃ nanoparticles.

Two strategies involving hydrothermal synthesis and SiO_2-templating were employed to fabricate traditional In_2O_3 nanoparticles with InOH•••In FLPs. In the first method, 0.6 mmol of $In(NO_3)_3 \cdot xH_2O$ and 17 mL of DI water were added to a 25 mL stainless-steel autoclave, following the same treatment process as described above to obtain the $In(OH)_3$-nanoparticle precursor. The precursor was then calcined for 5 h at 300 °C in air condition, resulting in a sample labeled as H-IO. As for the second method, SiO_2 microspheres was first synthesized by the Stöber method using TEOS in a mixed solution of ammonia and ethanol. Next, 1.2 g $In(NO_3)_3 \cdot xH_2O$ and 4.8 g SiO_2 microspheres were mixed in 30

ml of DI water with sonicating and magnetic stirring for 1 h to ensure homogeneity. The solution was then dried at 80 °C for about 12 h, and the resulting solid was directly calcined at 300 °C for 3 h. During this process the sample turned from white to pale yellow, indicating the formation of In_2O_3. The In_2O_3/SiO_2 mixture was ground, and dispersed in 2 M NaOH (50 times× excess by mass) to remove the SiO_2 by base etching at 80 °C while stirring for 24 h. Then the suspension was filtered and washed with DI water to ensure thorough removal of any trapped impurities before being dried at 60 °C for 12 h in a vacuum oven. The resulting sample was labeled as Si-IO after grinding.

1.1.3. *Synthesis of amine-modified In_2O_3 nanoparticles.*

The amine-modified In_2O_3 nanoparticles were synthesized by an impregnation method. 0.2 g of the prepared H-IO or Si-IO samples was added to 15 mL of EDA, and stirred at room temperature for 3 hours. Then the samples were centrifuged and washed for three times each with ethanol and deionized water. After that they were dried at 60 °C about 12 h in a vacuum oven. The obtained products were labeled as E-H-IO and E-Si-IO respectively. Additionally, to prevent the removal of EDA during the washing process, another portion of the impregnated H-IO samples were directly dried without undergoing the washing process, labeled as EI-H-IO.

1.2. Characterizations of In_2O_3 Catalysts.

Power X-ray diffraction (PXRD) patterns were recorded on a Miniflex600 diffractometer (Rigaku, Japan) with Cu Kα radiation (λ = 0.15418 nm) in step mode between 10 ° to 70 °. SEM images were obtained on a JEOL JSM 6700F instrument (Japan) with an accelerating voltage of 5 kV. The obtained samples were also characterized by Sigma 500 VP (Carl Zeiss AG) field emission scanning electron microscope (FESEM) and EDS. Transmission electron microscope (TEM), high-resolution transmission electron microscope (HRTEM) images and selected area electron diffraction (SAED) pattern were examined on a JEM-2100 microscope (Japan) at 200 kV. The Brunauer-Emmet-Teller (BET) adsorption and desorption isotherm of N_2 and the adsorption and desorption isotherm of CO_2 were determined on a Kubo X1000 BET analyzer (China) at 77 K and 298 K, respectively, after a pretreatment of samples at 120 °C for 2 h. Fourier Transform Infrared (FT-IR) spectra were recorded on a NEXUS-470 spectrometer (Thermo Nicolet, USA). Ultraviolet–visible diffused reflectance spectra (UV–vis DRS) were tested on a Shimadzu UV-2600i spectrophotometer equipped with an integrating sphere attachment in the wavelength range of 220~800 nm. X-ray photoelectron spectra (XPS) measurements were performed on a ESCALAB 250Xi photoelectron spectroscopy (Thermo

Fisher Scientific, USA) at 1.0×10^{-9} mbar with monochromatic Al Kα radiation. The XPS analyses were conducted at a test energy of 1486.6 eV, using a spot size of 500 μm. The XPS instrument was operated at a tube voltage of 15 kV and a tube current of 10 mA. Additionally, all the obtained binding energies were corrected with reference to C 1s peak at 284.8 eV. The solid-state nuclear magnetic resonance (NMR) experiment of high-resolution ^{13}C solid-state spectra was recorded using the ramp ^{13}C magic angle spinning (MAS) sequence at room temperature in a Bruker Avance III HD 400HMz spectrometer equipped with a double resonance solid probe (Bruker, Germany). Isotope tracing experiments were performed using $^{13}CO_2$, and the isotope product gases were measured on a Hiden HPR-20 EGA mass spectrometer (Hiden Analytical, UK). Thermogravimetry-mass spectrum analysis (TG-MS, Rigaku, Japan) was s detected on a Thermo plus EV2/Thermo mass photo analyzer from 30 to 800 °C with a heating rate of 10 °C/min in an argon atmosphere. Room-temperature electron spin resonance (EPR) spectra were determined on an A300 ESR spectrometer (Bruker, Germany). CO_2 temperature programmed desorption (CO_2-TPD) measurements were operated on AMI-300 chemisorption analyzer (Altamira Instruments, USA). Room temperature photoluminescence (PL) spectra were obtained a FS5 photoluminescence spectroscopy (Edinburgh Instruments, UK). Additionally, transient photocurrent response and Mott-Schottky analysis were conducted on a CHI660E electrochemical analyzer (CH Instrument, USA) with the former utilizing a 500W Xe lamp (CEL-PF300-T8, China). Electrochemical impedance spectrum measurements were conducted on an Autolab 302A electrochemical analyzer (Metrohm, Switzerland). 0.1 M sodium sulfate electrolyte was used in in the entire electrochemical and photoelectrochemical characterization procedures.

1.3. Catalytic Performance Tests.

Gas-phase photocatalytic rate measurements were performed using a flow reaction system. As depicted in Figure S6, a dedicated quartz tube was utilized to contain approximately 100 mg of the sample, which was positioned in the central flat region of the tube and sealed with quartz wool at bottom. The reaction system was supplied with a gas mixture consisting of 6 mL min⁻¹ of H_2 and 2 mL min⁻¹ of CO_2 ($H_2 : CO_2 = 3$), introduced into the gas path before connecting the quartz tube to the reaction setup and placing it in a heating furnace. The reactor temperature was controlled using an OMEGA temperature controller, with a thermocouple sensor in contact with the sample. Irradiation was carried out using an CEL-PF300-T8 Xe lamp at an optical density of 500 mW cm⁻². The product gases were analyzed using a GC-7920 gas chromatograph (GC) equipped with a flame ionization

detector (FID). The GC had two gas analysis channels: FID1 (ZKAT-PLOT Pora Q column) for hydrocarbon detection (CH_4 and CH_3OH), and FID2 (TDX-01 column) for CO and CO2 detection. Both channels employed N_2 as the carrier gas.

1.4. *In-situ* DRIFTS of Adsorption Measurement

1.4.1. In-situ DRIFTS spectra of the adsorption of CO_2.

In-situ DRIFTS experiments were performed on a Tensor II spectrometer (Bruker, Germany) equipped with a mercury-cadmium-telluride (MCT) detector. Prior to measurement, the catalysts were purged with argon at 250°C for 0.5 h. The background spectrum was obtained at 250 °C in argon flow with a resolution of 4 cm^{-1}. Subsequently, the catalysts were exposed to a mixture of CO_2 and argon (5 mL min^{-1} CO_2, and 55 mL min^{-1} Ar) under dark conditions for different times. The *in-situ* DRIFT spectra were recorded by collecting enough scans at a resolutions of 4 cm^{-1} until the spectrums were stabilized.

1.4.2. In-situ DRIFTS spectra of surface species under reaction conditions.

Prior to the formal signal acquisition during the reaction, a feed gas mixture of CO_2, H_2 and Argon (5 mL min^{-1} CO_2, 15 mL min^{-1} H_2 and 30 mL min^{-1} Ar) was introduced. After the infrared absorption spectrum of the sample reached stability, background spectrum was collected. Subsequently, illumination was introduced during the reaction to initiate the collection of infrared absorption spectrum. The *in-situ* DRIFT spectra were recorded by collecting enough scans at a resolutions of 4 cm^{-1} until the spectrums were stabilized.

1.5. Theoretical Calculations

The density functional theory (DFT) calculations were performed using the Cambridge Sequential Total Energy Package (CASTEP) computational codes. During the geometry optimization, lattice parameters and atomic positions were optimized simultaneously. Based on the experimental data, the grafting state model of EDA on surface of In_2O_3 was established by replacing one hydroxyl group on the surface of In_2O_3 with one amine group of EDA molecule. Additionally, one of the oxygen atoms coordinating with the amine group-coordinated indium atom was removed to establish $InNH_2$•••In models. For calculating the electronic structures and density of states, the geometry optimization of (110) crystal face of In_2O_3, In_2O_{3-x}, $In_2O_{3-x}(OH)_y$, and $In_2O_{3-x}(EDA)_y$ were calculated by the PBE method within Generalized Gradient-corrected Approximation (GGA) with the exchange-correlation potential. The Vanderbilt ultrasoft pseudopotential with a cutoff energy of 340 eV was used to ensure

the precision of the results. Brillouin zone integration was represented using the K-point sampling scheme of 2×2×2 Monkhorst−Pack scheme. The convergence tolerance for geometry optimization was selected with the differences in total energy ($1.0×10^{-5}$ eV/atom), the maximal ionic Hellmann−Feynman force ($3.0×10^{-2}$ eV/Å), the stress tensor ($5.0×10^{-2}$ GPa), and the maximal displacement ($1.0×10^{-3}$ Å).
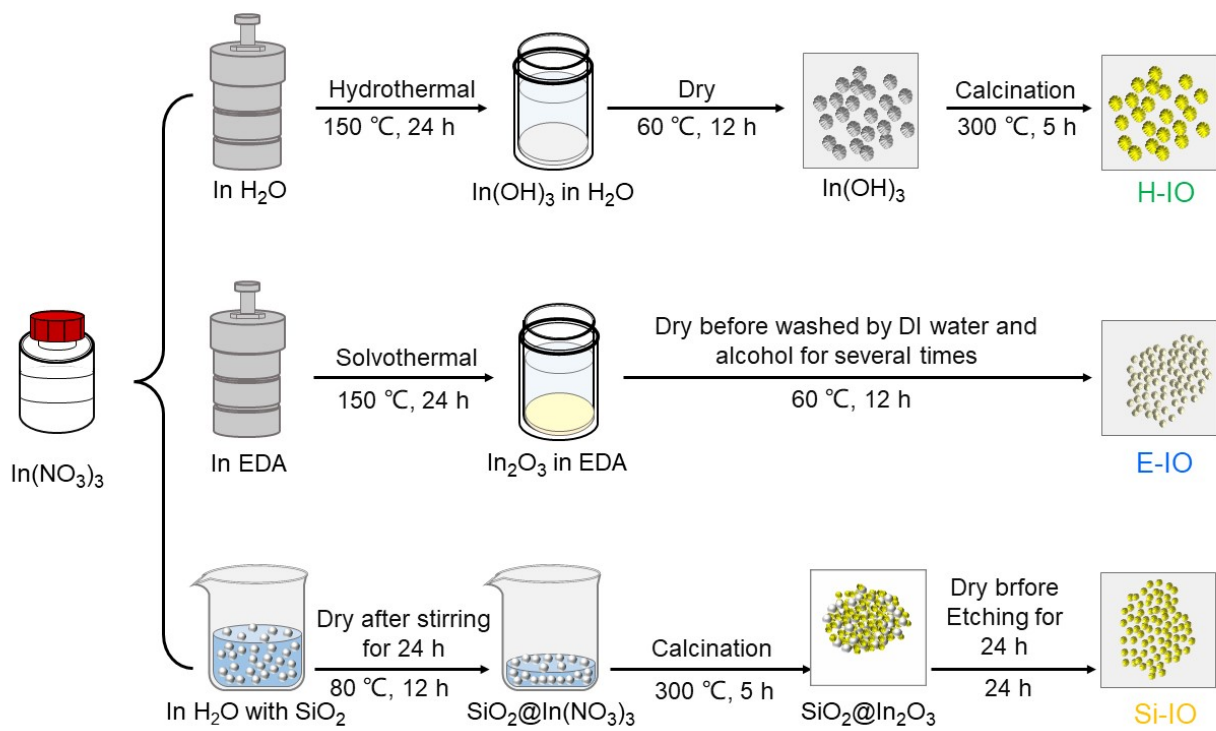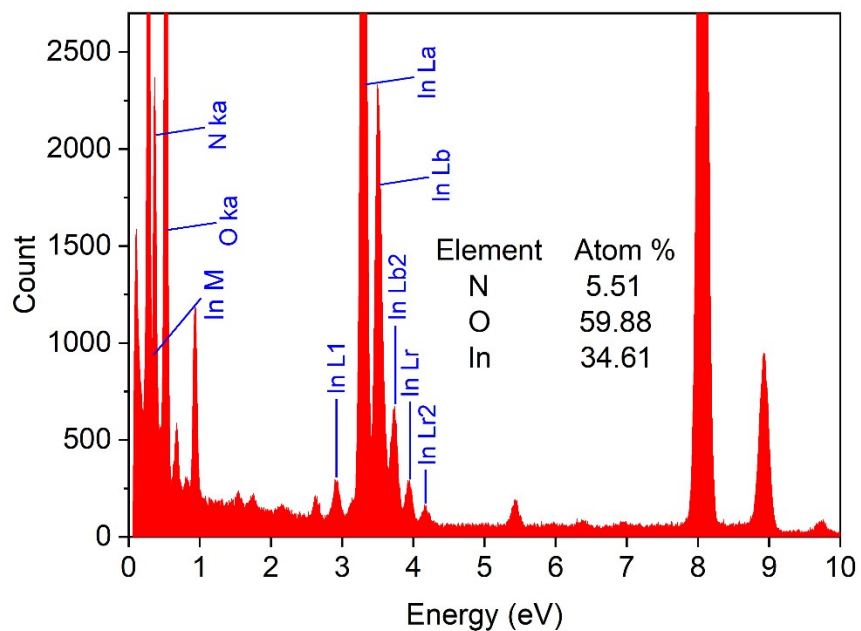
Scheme S1. Schematic illustration of the synthesis of H-IO, E-IO and Si-IO.

Figure S1. EDS spectrum of E-IO.
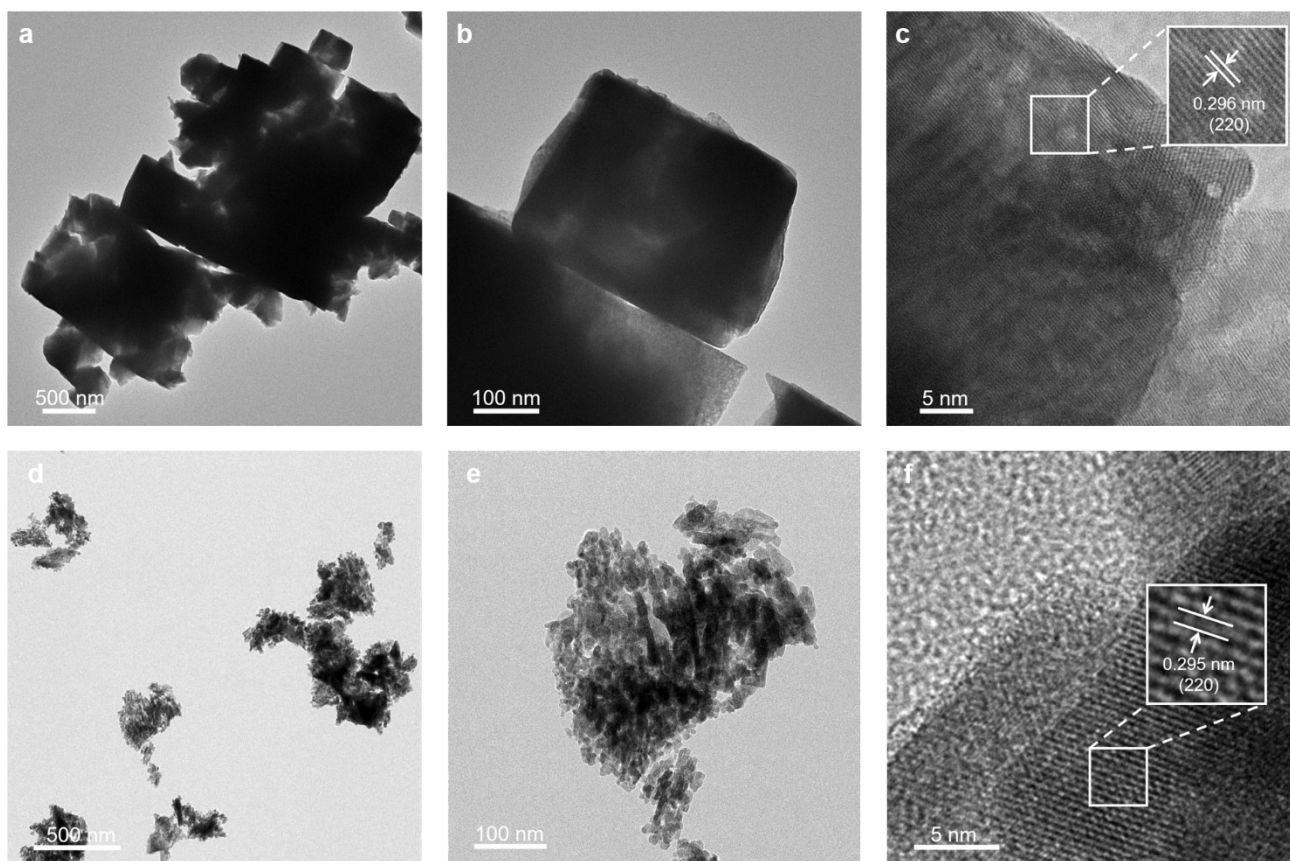
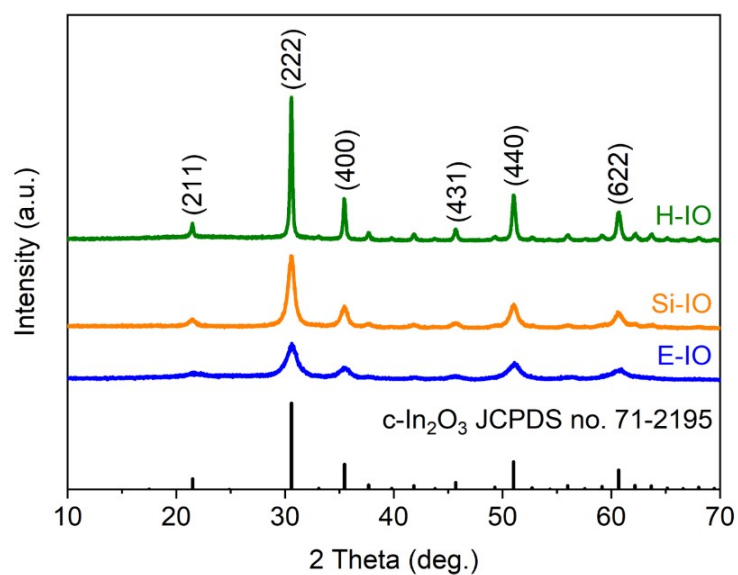**Figure S2.** TEM and HRTEM images of (a-c) H-IO and (d-f) Si-IO.

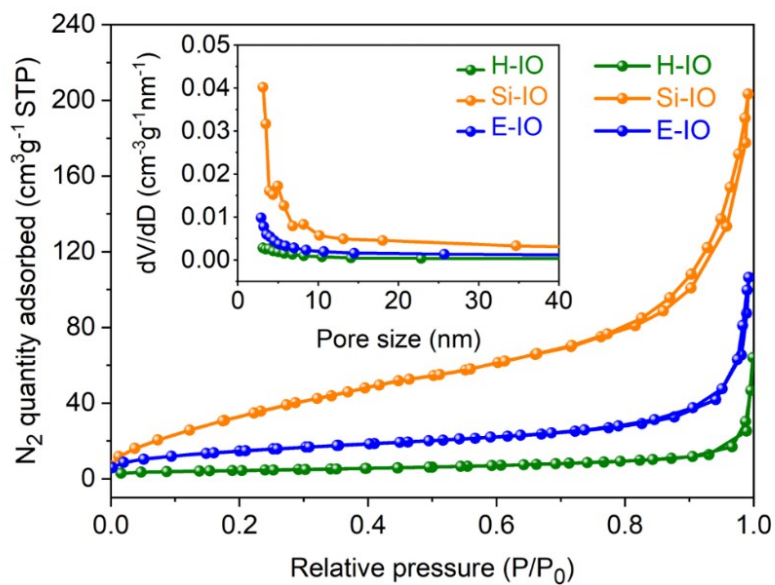**Figure S3.** Powder X-ray diffraction patterns of H-IO, Si-IO and E-IO.

Figure S4. N_2 adsorption−desorption isotherms and pore diameter distributions (inset) of all three catalysts.
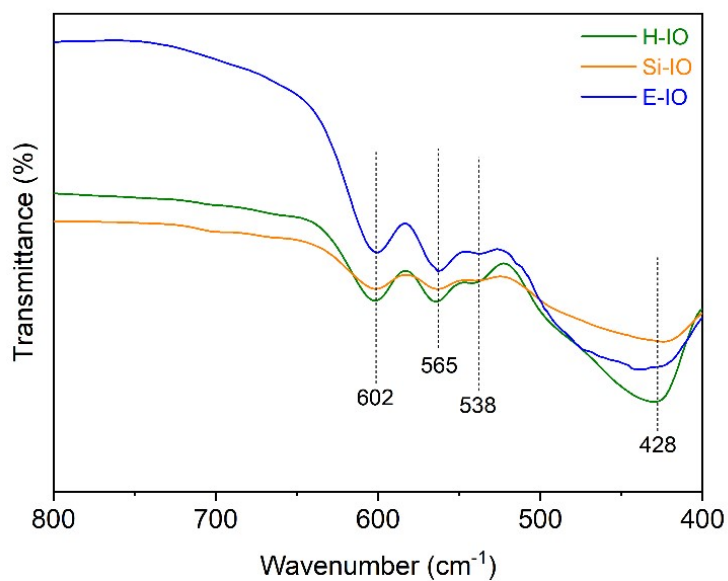

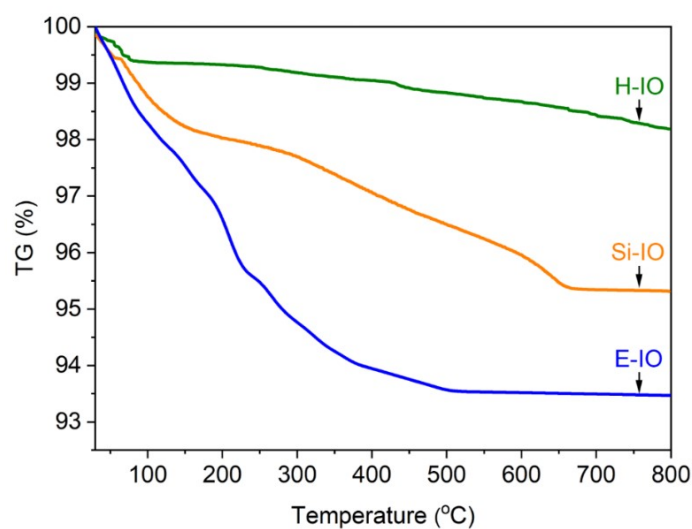**Figure S5.** FTIR spectra of H-IO, Si-IO and E-IO between 800 ~ 400 cm⁻¹.

Figure S6. TG curves of H-IO, Si-IO and E-IO in air condition.
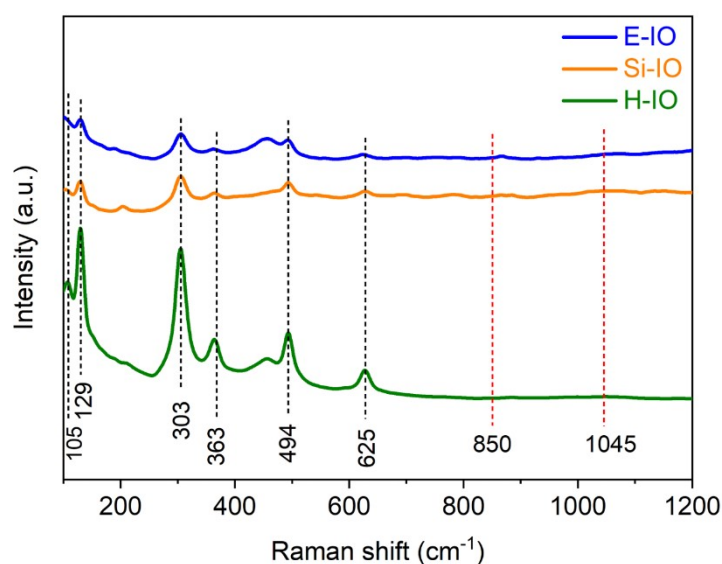

Figure S7. Raman spectra of H-IO, Si-IO and E-IO. All these peaks between 625~105 cm^{-1} are attributed to the vibration mode of Body Centered Cubic (BCC) structured In_2O_3 crystals.[1] According to the previous literature, the peaks around 1045 cm^{-1} and 850 cm^{-1} are attributed to the characteristic peaks of nitrate ion (NO_3^-).[2,3] However, for all the three samples, there are no characteristic peaks related to NO_3^- observed.
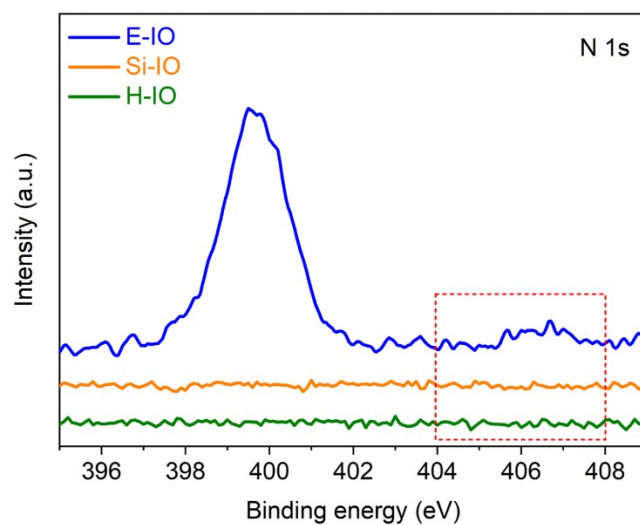
Figure S8. High resolution N 1s XPS spectra of the three samples. According to the previous literature, the peaks around 404 eV and 408 eV are attributed to the characteristic peaks of nitrate ion (NO_3^-).[2, 4, 5] However, for all the three samples, there are no characteristic peaks related to NO_3^- observed.
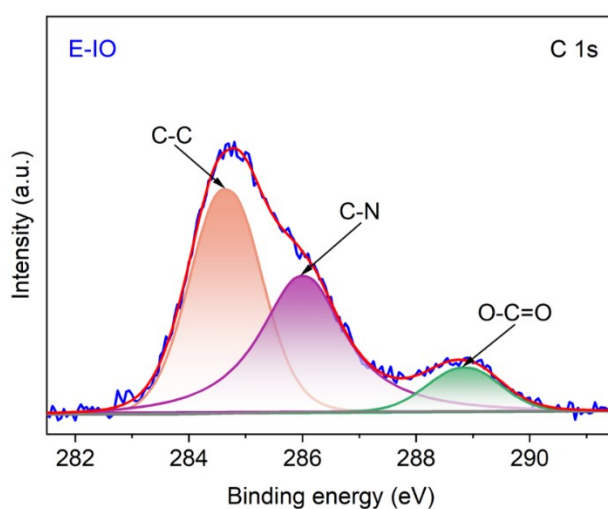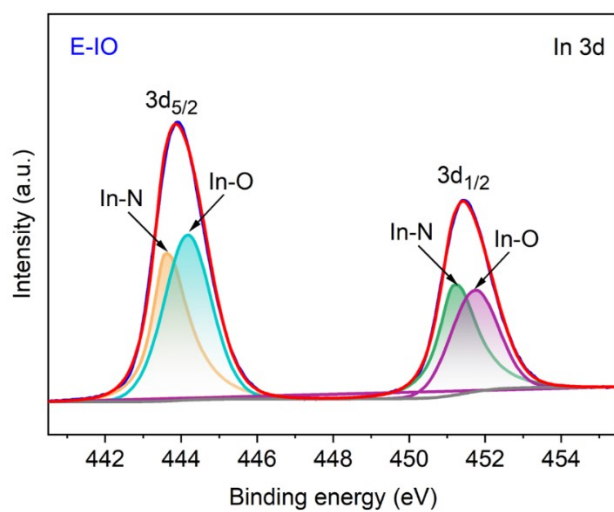

Figure S9. High resolution C 1s XPS spectra of the E-IO.

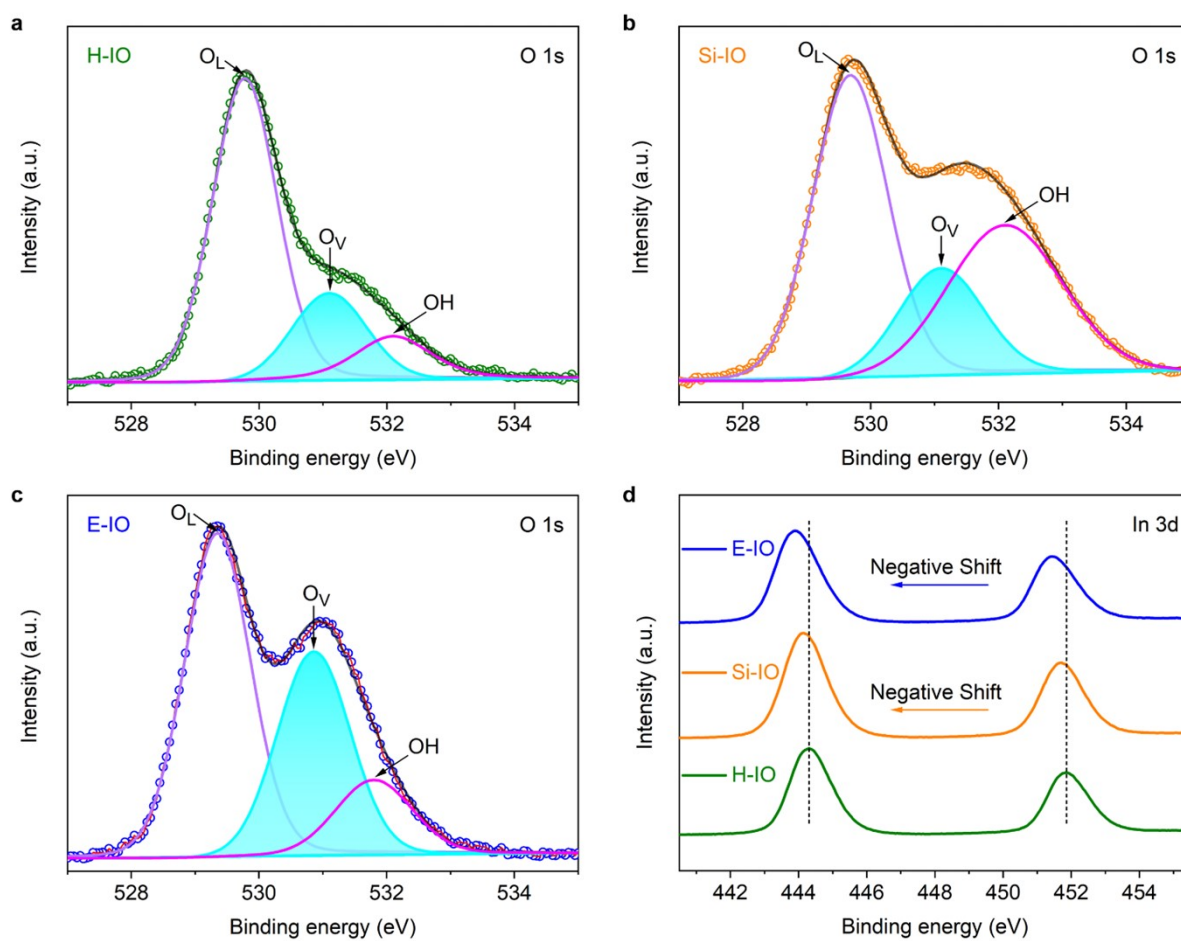**Figure S10.** High resolution In 3d XPS spectra of the E-IO.

Figure S11. High-resolution O 1s XPS spectra of (a) H-IO, (b) Si-IO and (c) E-IO. (d) High resolution In 3d XPS spectra of the three samples.
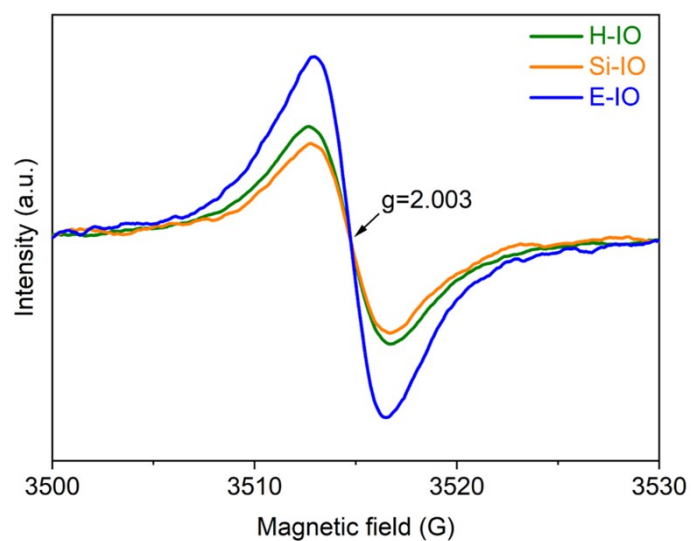
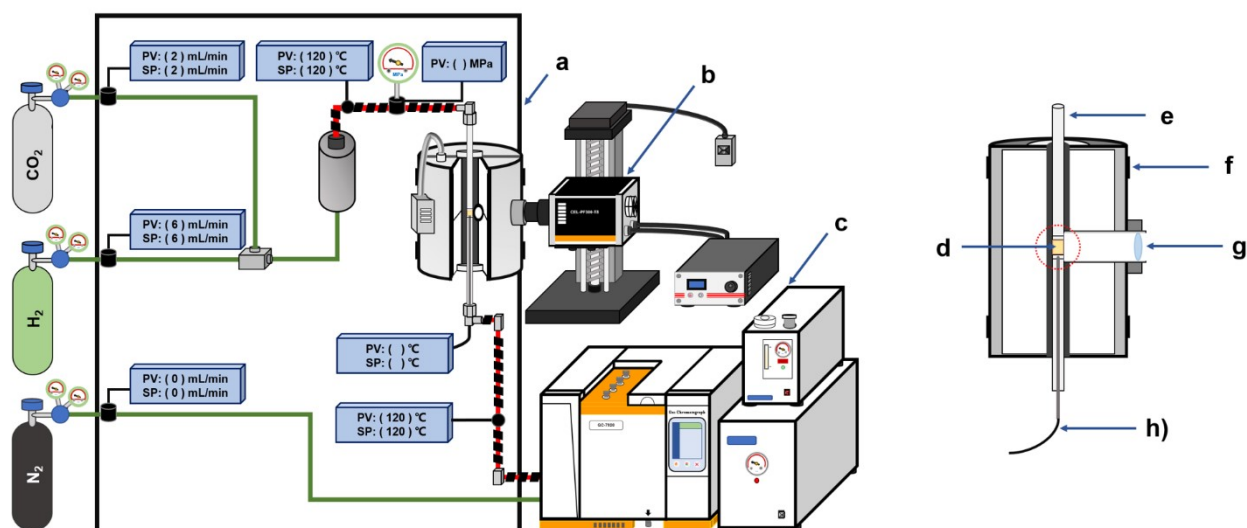**Figure S12.** EPR curves of the three samples.

Figure S13. Schematic diagram of the miniaturized photothermal catalytic micro-reactor system. (a) Photothermal catalytic system; (b) Xe lamp; (c) gas chromatography; (d) catalyst; (e) quartz tube; (f) the heating furnace; (g) quartz condenser window; (h) thermocouple sensor.
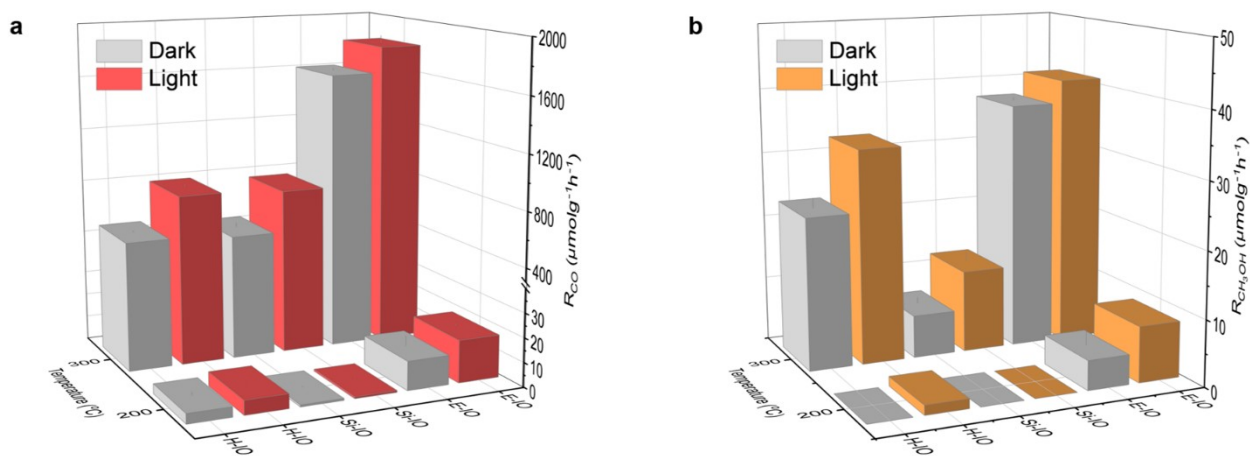
Figure S14. (a) CO production rate at 200 and 300 °C with and without solar irradiation. (b) CH$_3$OH production rate at 200 and 300 °C with and without solar irradiation.

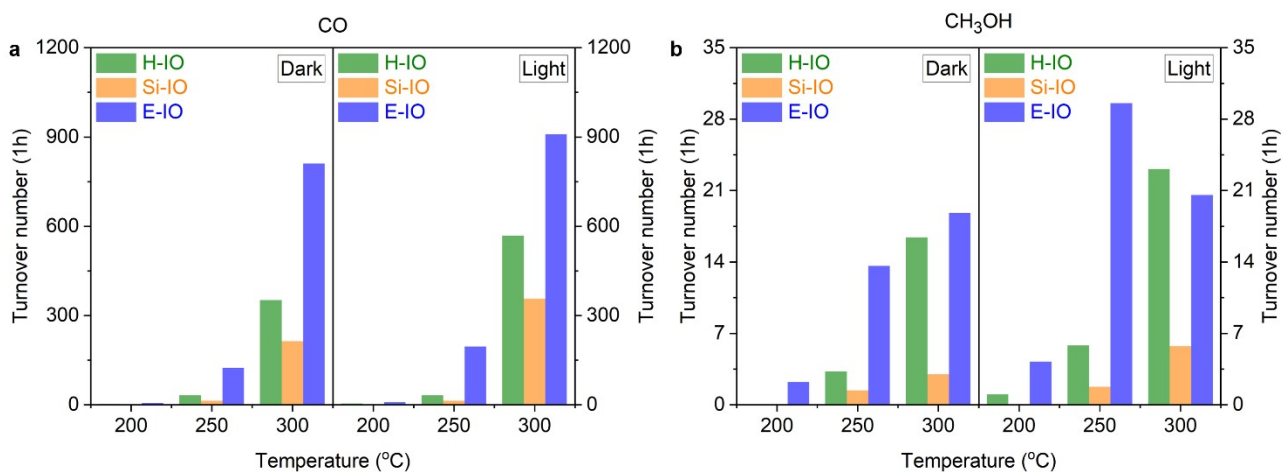**Figure S15.** Turnover number (TON) of the three samples to produce (a) CO and (b) CH$_3$OH at 200, 250 and 300 °C with and without solar irradiation.
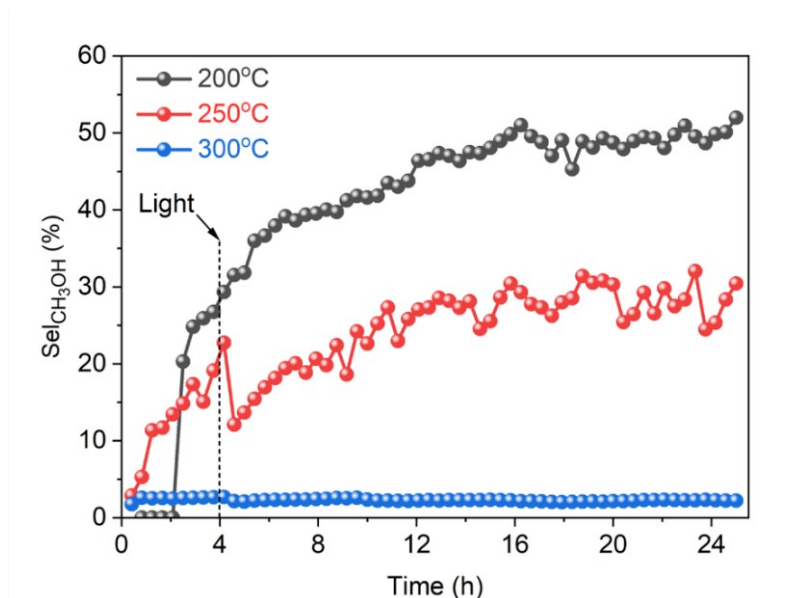
14

Figure S16. Long-term (24 h) catalytic stability of E-IO nanoparticles in catalyzing hydrogenation of CO_2 with light irradiation; reaction condition: 250 °C, 6 mL min^{-1} H_2 and 2 mL min^{-1} CO_2.

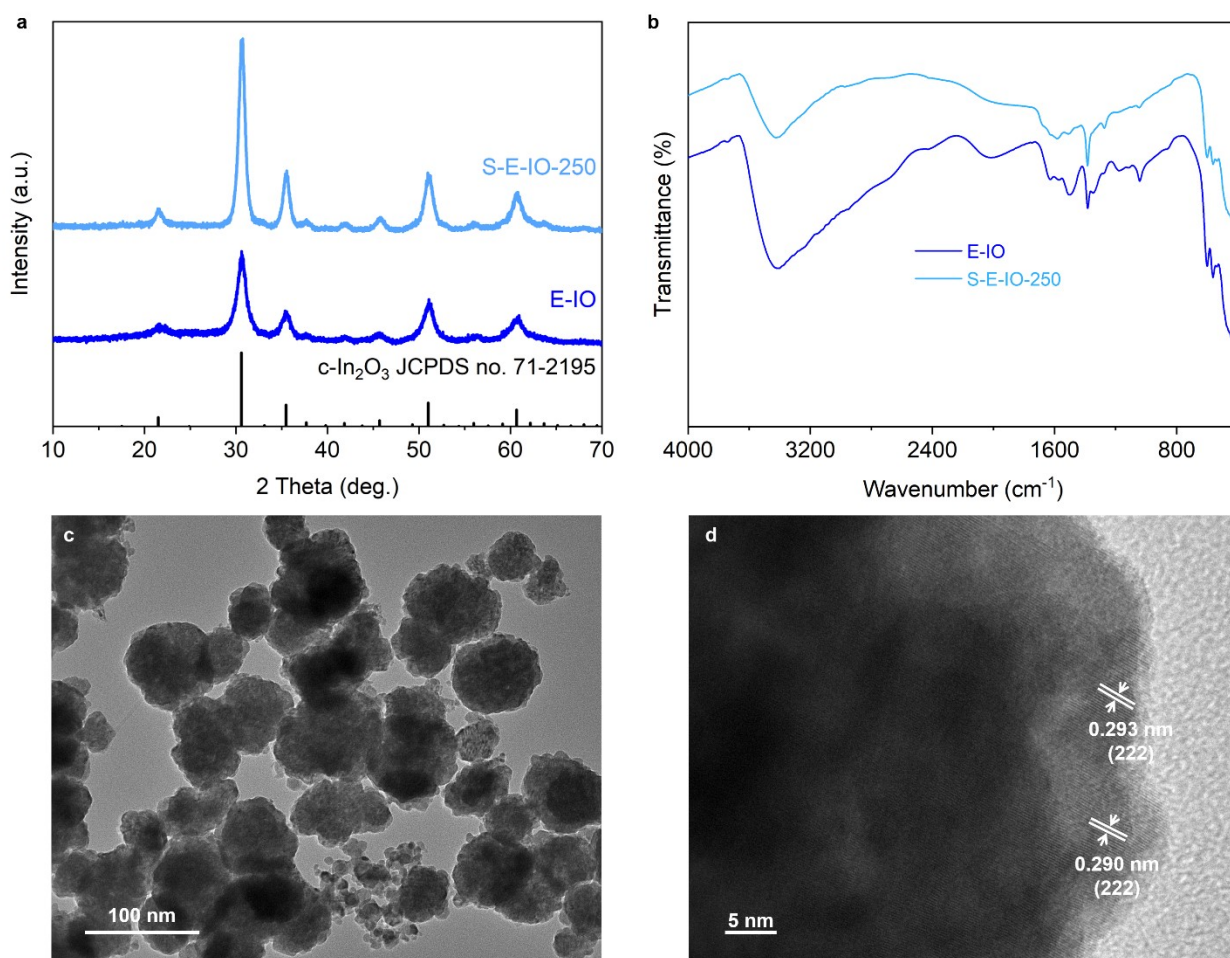**Figure S17.** Characterizations of spent E-IO (S-E-IO) catalyst after 24 h of photocatalytic CO_2 hydrogenation at 250 °C. (a) Powder X-ray diffraction patterns; (b) FTIR spectra; (c-d) TEM and HRTEM images.

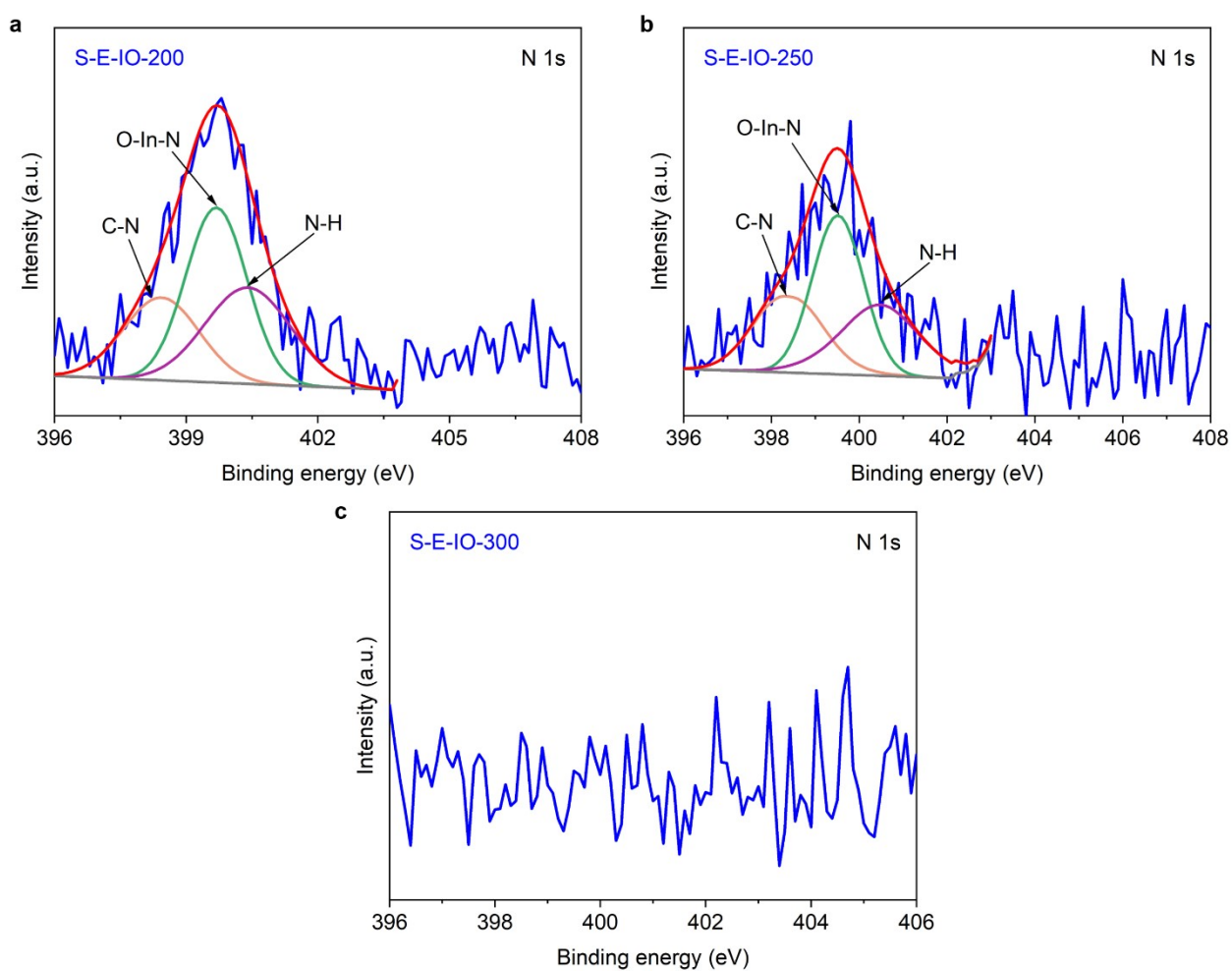**Figure S18.** High-resolution N 1s XPS spectra of the spent E-IO after catalytic reaction at (a) 200 °C (S-E-IO-200), (b) 250 °C (S-E-IO-250) and (c) 300 °C (S-E-IO-300), respectively.
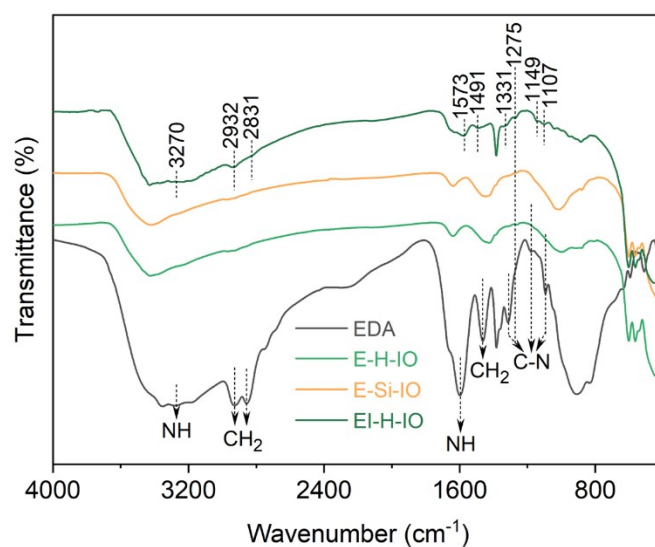
Figure S19. FTIR spectra of E-H-IO, E-Si-IO and EI-H-IO.
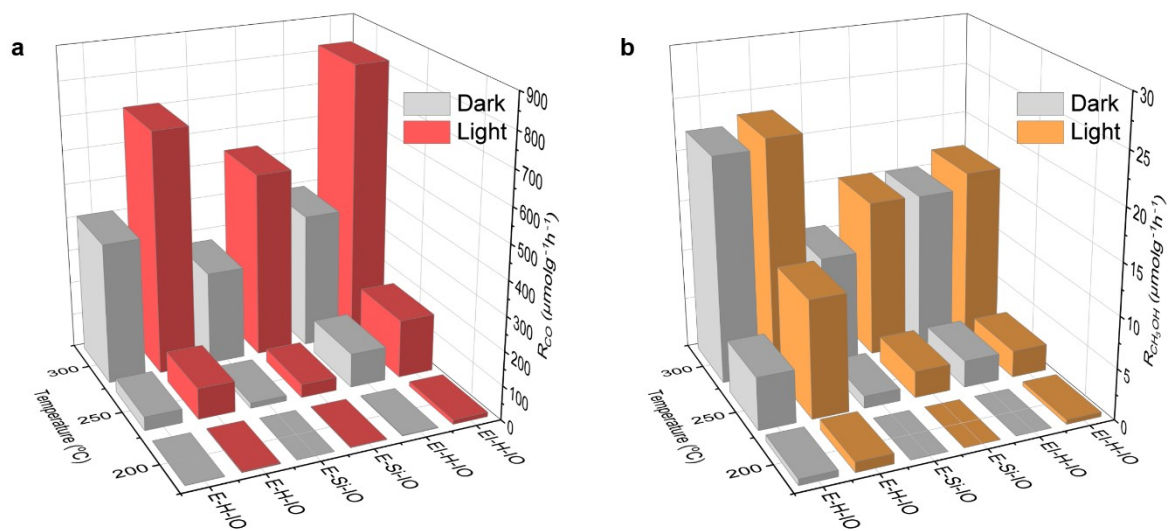
Figure S20. (a) CO and (b) CH_3OH production rates at different reaction temperatures for amine-modified In_2O_3 (E-H-IO, E-Si-IO and EI-H-IO), with and without solar irradiation.
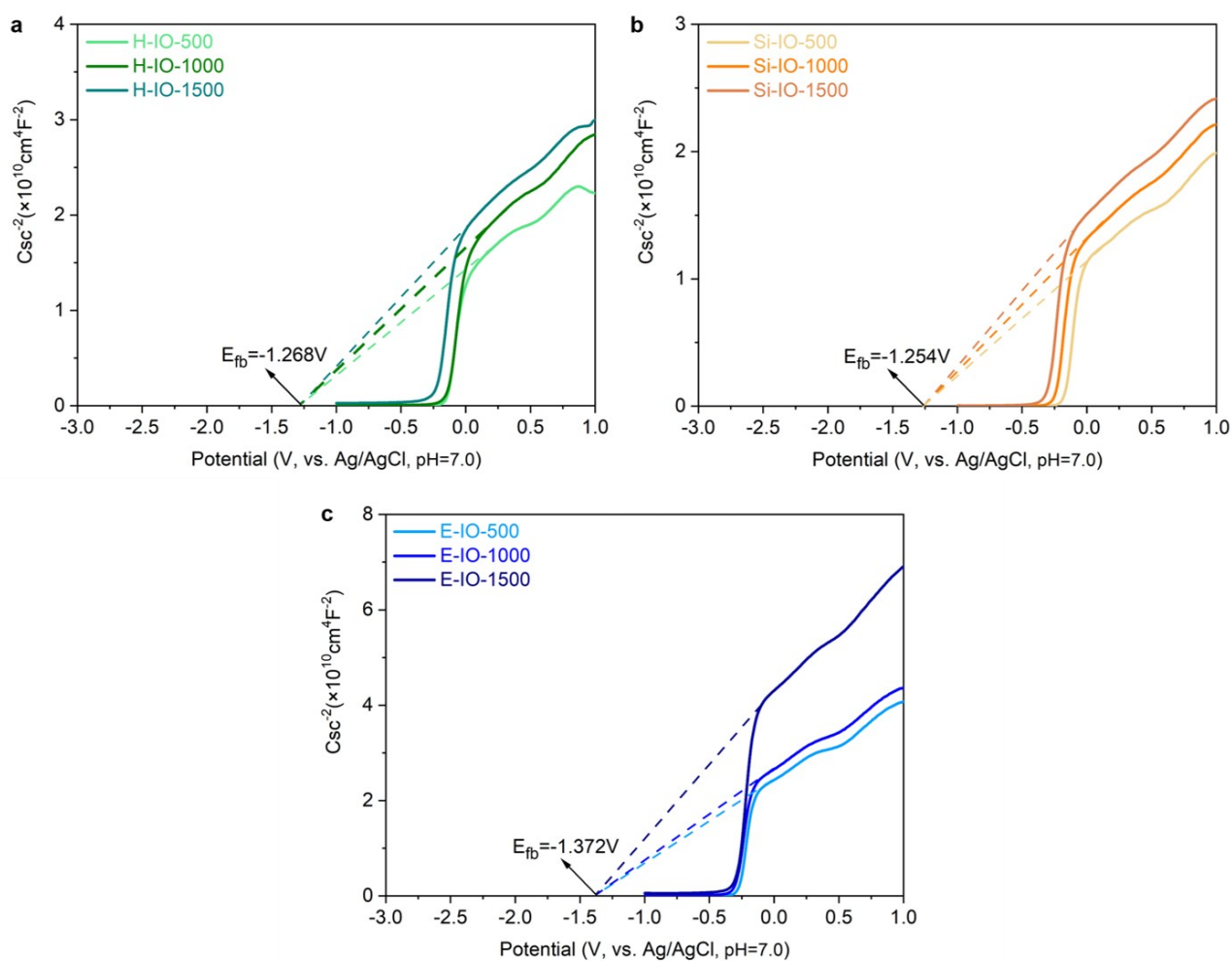
Figure S21. Mott−Schottky plots of (a) H-IO, (b) Si-IO and (c) E-IO.
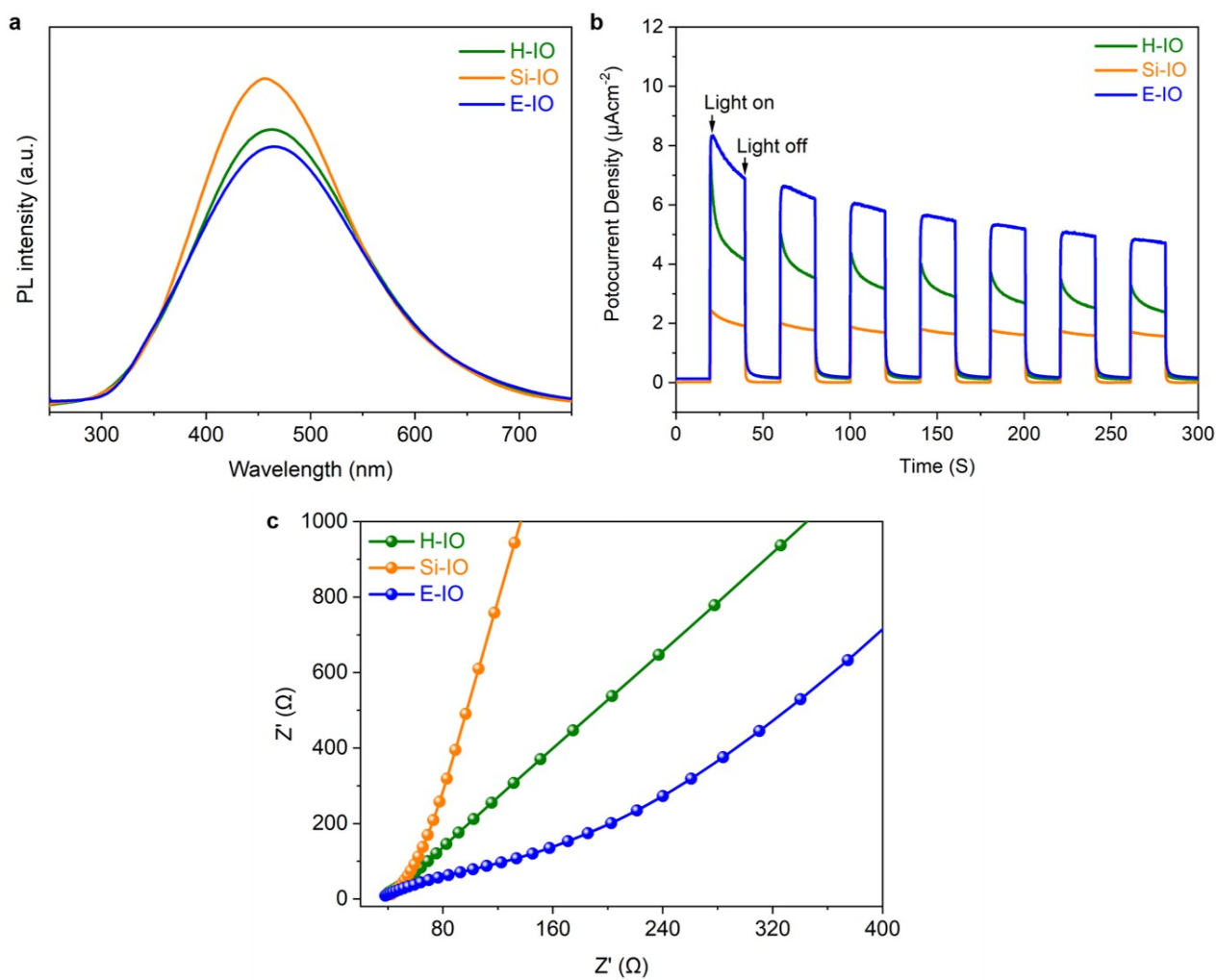
Figure S22. Photoelectric chemical characterizations of H-IO, Si-IO and E-IO. (a) Room-temperature PL spectrum using an excitation wavelength of 224 nm; (b) transient photocurrent response and (c) EIS spectra in a 0.5 M sodium sulfate solution.
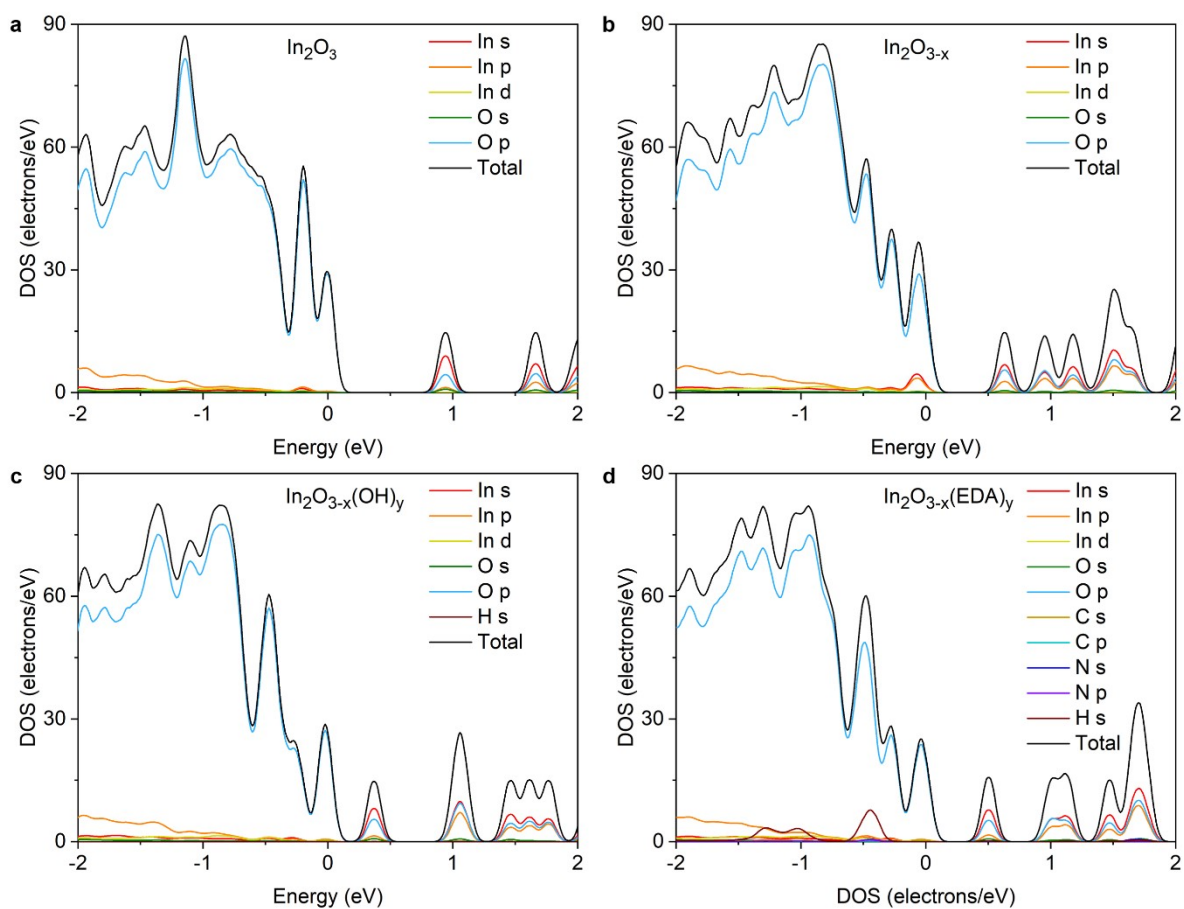
Figure S23. Effect of O_V, OH defects and NH_2 groups on the PDOS for various indium oxide (110) surfaces. (a) Pristine, defect-free In_2O_3 surface. (b) In_2O_{3-x} surface containing only an oxygen vacancy (O_V) defect. (c) $In_2O_3\text{-x}(OH)_y$ surface containing both O_V and OH defects. (d) $In_2O_{3-x}(EDA)_y$ surface containing both O_V and NH_2 group.

Figure S24. *In-situ* DRIFTS spectra for the adsorption of CO_2 on (a) H-IO, (b) Si-IO, and (c) E-IO, respectively, within 40 minutes.

Figure S25. *In-situ* DRIFTS spectra for CO_2 hydrogenation under light conditions on (a) H-IO and (b) Si-IO.

Table S1. Comparison of various microscopic parameters of different catalysts.

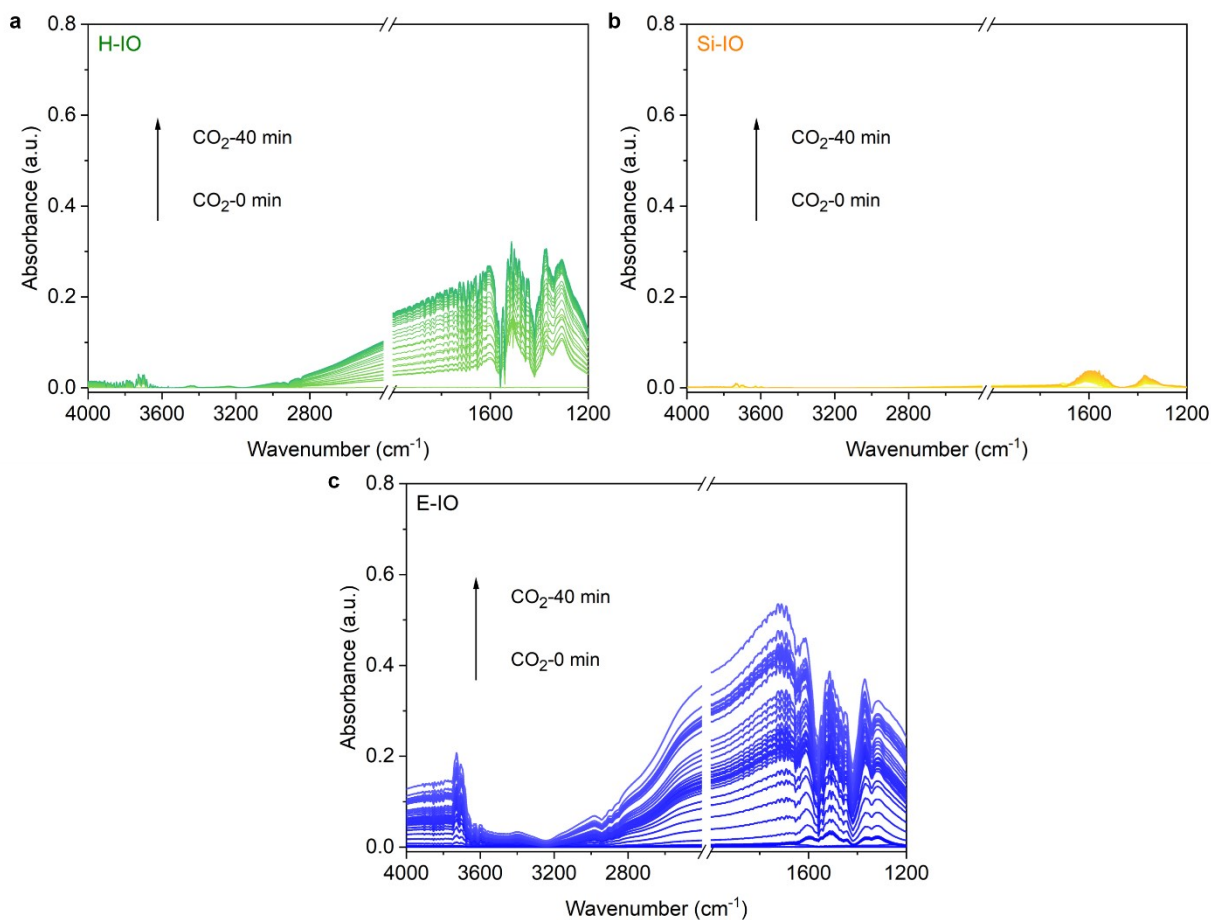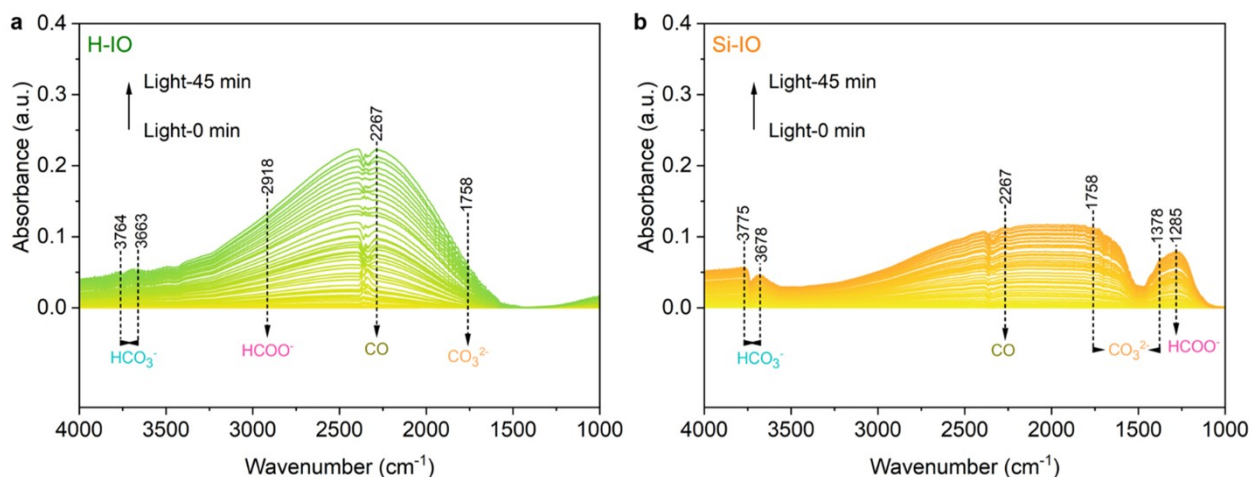| Sample	Crystallite size[a] D_{XRD}(nm)	Surface area[b] ($m^2 g^{-1}$)	Crystallite size[c] D_{TEM}(nm)	Mean pore size[d] (nm)	Atomic content[e] (%)			
					In	O	N	Si
H-IO	29.95	15.67	29.02	3.13	36.71	63.29	0	0
Si-IO	9.47	94.97	9.68	3.13	23.23	65.23	0	11.54
E-IO	6.41	50.54	6.50	2.89	31.55	63.27	5.18	0

[a] Crystallite size from *Scherrer* formula.

[b & d] Obtained from BET method.

[c] Measured by TEM images.

[e] Obtained from XPS method.

Table S2. N 1s binding energy for the various species.

Zone	Binding energy (eV)	Species	References
N 1s	404.90~407.50	$M\text{-}NO_3^-$	[2, 4, 5]
N 1s	403.60~405.20	$M\text{-}NO_2^-$	[4, 5]
N 1s	399.10~400.10	M-NO	[5, 6]
N 1s	396.30	N^{3-}	[4]
N 1s	401.80~402.00	NH_3^+	[2, 7, 8]
N 1s	400.10~400.70	NH_2	[7, 8]
N 1s	~399.50	O-M-N	[9, 10]
N 1s	399.49~399.73	M-NHR	[11]
N 1s	399.30~399.70	$C\text{-}NH_2$	[11, 12]
N 1s	398.50~398.70	C-N	[2, 12]

The M used in the table is referred to metallic ions.

References

1. C. Shi, J. Liu, W. Li, X. Jiang, H. Yang and Q. Liu, *Ceram. Int.*, 2018, **44**, 22235-22240.
2. Z. Ren, X. Xu, X. Wang, B. Gao, Q. Yue, W. Song, L. Zhang and H. Wang, *J. Colloid Interface Sci.*, 2016, **468**, 313-323.
3. P. M. Castro and P. W. Jagodzinski, *Spectrochim. Acta A*, 1991, **47**, 1707-1720.
4. J. Baltrusaitis, P. M. Jayaweera and V. H. Grassian, *Phys. Chem. Chem. Phys.*, 2009, **11**, 8295-8305.
5. J. L. Hueso, J. P. Espino´s, A. Caballero, J. Cotrino and A. R. Gonza´lez-Elipe, *Carbon*, 2007, **45**, 89-96.
6. N. Wang, H. Song, H. Ren, J. Chen, M. Yao, W. Huang, W. Hu and S. Komarneni, *Chem. Eng. J.*, 2019, **358**, 531-539.
7. V. Hernández-Morales, R. Nava, Y. J. Acosta-Silva, S. A. Macías-Sánchez, J. J. Pérez-Bueno and B. P. c, *Microporous and Mesoporous Mater.*, 2012, **160**, 133-142.

8. K. Kishi, *J. Electron Spectros. Relat. Phenomena*, 1998, **46**, 237-247.

9. M. Yao, B. Sun, N. Wang, W. Hu and S. Komarneni, *Appl. Surf. Sci.*, 2019, **480**, 655-664.

10. W. Li, F. Xia, J. Qu, P. Li, D. Chen, Z. Chen, Y. Yu, Y. Lu, R. A. Caruso and W. Song, *Nano Research*, 2014, **7**, 903-916.

11. I. Losito, E. D. Giglio, N. Cioffi and C. Malitesta, *J. Mater. Chem.*, 2001, **11**, 1812-1817.

12. M. Tabbal, P. Merel, S. Moisa, M. Chaker, E. Gat, A. Ricard, M. Moisan and S. Gujrathi, *Surf. Coat. Technol.*, 1998, **98**, 1092-1096.